1 *Review*

2 Three Dimensional ZnO Hierarchical Nanostructures:
3 Solution Phase Synthesis and Applications

4 **Xiaoliang Wang [1,*], Mashkoor Ahmad [2] and Hongyu Sun [3,*]**

5 [1] College of Science, Hebei University of Science and Technology, Shijiazhuang 050018, PR China;
6   wxlsr@126.com (X. W.)
7 [2] Nanomaterials Research Group, Physics Division, Pakistan Institute of Nuclear Science and Technology,
8   P.O. Nilore, Islamabad 44000, Pakistan; mashkoorahmad2003@yahoo.com (M. A.)
9 [3] Department of Micro- and Nanotechnology, Technical University of Denmark, Kongens Lyngby 2800,
10   Denmark; hsun@nanotech.dtu.dk (H. S.)
11 * Correspondence: wxlsr@126.com; hsun@nanotech.dtu.dk; Tel.: +45-45 25 68 40 (H. S.)

12 **Abstract:** Zinc oxide (ZnO) nanostructures have been studied extensively in the past years due to
13 the novel electronic, photonic, mechanical and electrochemical properties. Recently, more attention
14 has been paid to assemble nanoscale building blocks into three dimensional (3D) complex
15 hierarchical structures, which not only inherit the excellent properties of the single building blocks
16 but also provide potential applications in the bottom-up fabrication of functional devices. This
17 review article focuses on 3D ZnO hierarchical nanostructures, and summarizes major advances in
18 the solution phase synthesis, applications in environment, and electrical/electrochemical devices.
19 We present the principles and growth mechanisms of ZnO nanostructures via different solution
20 methods, with an emphasis on rational control of the morphology and assembly. We then discuss
21 the applications of 3D ZnO hierarchical nanostructures in photocatalysis, field emission,
22 electrochemical sensor, and lithium ion batteries. Throughout the discussion, the relationship
23 between the device performance and the microstructures of 3D ZnO hierarchical nanostructures
24 will be highlighted. This review concludes with a personal perspective on the current challenges
25 and future researches.

26 **Keywords:** zinc oxide; hierarchical nanostructures; solution phase synthesis; photocatalysis; field
27 emission; sensor; lithium ion batteries

28

29 1. Introduction

30   Advanced nanomaterials which are earth abundant and environmentally compatible show the
31 potential to solve the serious energy and environment problems. As an important and widely used
32 wide bandgap (3.0-3.2 eV) oxide semiconductor, ZnO shows unique physical and chemical
33 properties [1]. The applications of ZnO materials range from room temperature nanolasers,
34 nanogenerators, solar cells, lithium ion batteries and photocatalysts.
35   ZnO crystal shows the stable structure as hexagonal wurtzite under the condition of normal
36 temperature and atmospheric pressure. The crystal structure of ZnO can be viewed as a number of
37 alternating planes composed of tetrahedrally coordinated oxygen and zinc ions stacked alternately
38 along the [0001] direction (Figure 1). There are two important structural characteristics in wurtzite
39 ZnO, i.e., the absence of inversion symmetry of the positive and negative charge centers and polar
40 surfaces, which are the origin of piezoelectric properties and abundant 1D morphologies in the
41 synthesized ZnO nanostructures. In principle, the equilibrium morphology of a crystal is
42 determined by the standard Wulff construction, which dependents on the surface energy [2]. From
43 the viewpoint of decreasing the system total energy, low-index crystallographic faces prefer to be
44 exposed on the final crystallite as shown in Figure 1. Since the surface energy can be modified by
45 selective adsorption of additives or surfactants on specific planes, the morphology can be controlled
46 accordingly by adding suitable agents during the synthesis.

47

48
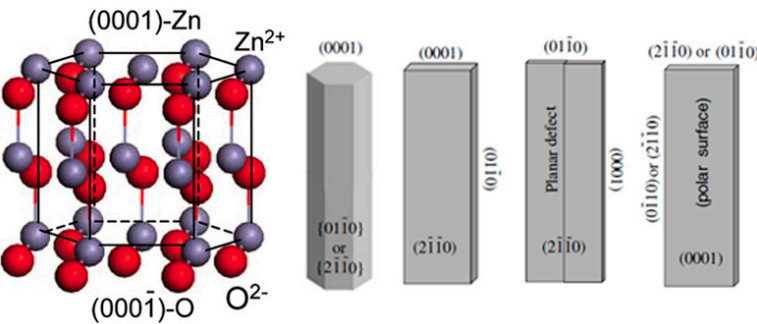
49   **Figure 1.** Crystal structure model of wurtzite ZnO, and typical morphologies of 1D ZnO
50   nanostructures with exposed facets.

51   Inspired by the size- or morphology-dependent properties or device performances, numerous
52   efforts have been devoted to the synthesis of ZnO nanostructures with 1D morphologies, such as
53   nanowires, nanobelts, nanorings, nanohelices and so on. Recently, more attention has been paid to
54   assemble low-dimensional nano-sized building blocks into three-dimensional (3D) complex
55   hierarchical structures [3]. Compared to mono-morphological structures, 3D ZnO hierarchical
56   structures usually exhibit high surface to volume ratios, a large accessible surface area and better
57   permeability. In addition, the hierarchical structures can increase the number of light traveling paths
58   and thereby facilitate light absorption. Finally, such 3D hierarchical structures not only inherit the
59   excellent properties of the single nano-sized building blocks but also provide potential applications
60   in the bottom-up fabrication of functional devices including photocatalysts, sensors and drug release
61   systems [4]. It is, therefore, important to develop facile approaches to synthesize 3D hierarchical
62   structures with controlled fashion.

63

64
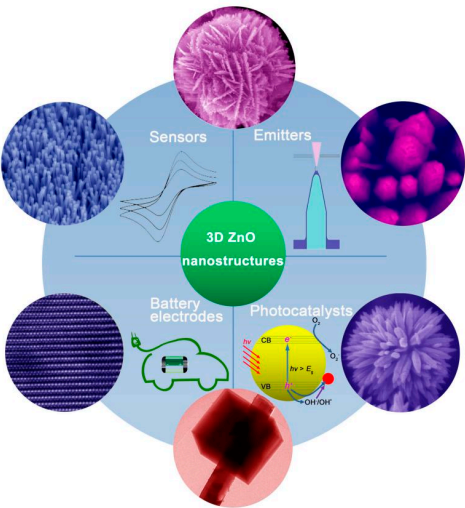
65   **Figure 2.** Typical 3D ZnO hierarchical nanostructures and their applications as photocatalysts, field
66   electron emitters, electrochemical sensors, and electrodes for batteries.

67   Herein, we summarize the most recent progress in the synthesis of 3D ZnO hierarchical
68   nanostructures by using solution phase routes, and discuss the related applications. Firstly, typical
69   solution phase synthesis methods towards 3D ZnO hierarchical nanostructures are reviewed,
70   including direct precipitation, microemulsions, hydrothermal/solvothermal, sol-gel, electrochemical
71   deposition, and chemical bath deposition. The basic principles of the synthesis and main factors
72   that influence the structure and morphology of the products are analyzed. Then, different
73   applications based on the 3D hierarchical architectures are discussed in the context of

74   photocatalysis, field emission, electrochemical sensors, and electrodes for lithium ion batteries
75   (Figure 2). Finally, current challenges and future outlooks of the synthesis and applications of 3D
76   ZnO hierarchical nanostructures are briefly outlined.

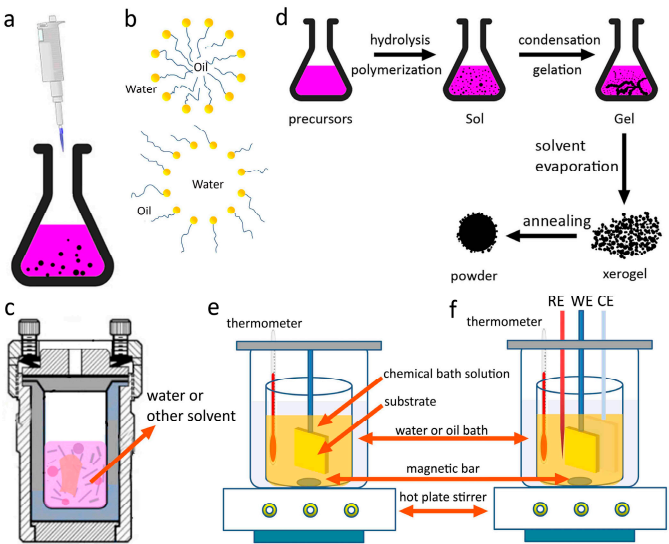## 2. Solution Phase Synthesis of 3D ZnO Hierarchical Nanostructures

78   The above discussion shows that the hierarchical assembly in ZnO nanostructures are related
79   to the electronic/optical properties and thus a wide range of potential applications. So far, many
80   synthesis strategies based on physical (physical and chemical vapor deposition, laser ablation, ball
81   milling, lithographic, etc), chemical (gas phase reaction, various solution phase synthesis), or
82   biological methods have been well established to obtain 3D ZnO hierarchical nanostructures [5].
83   Comparing to other methods, solution phase route shows unique advantages, such as low cost (low
84   in energy consumption and equipment costs), scalability, and ease of handling. Most of the solution
85   phase reactions occur under mild condition with a relatively low temperature (< 200 ^{o}C). Therefore,
86   solution phase synthesis have attracted increasing interest. Typical solution phase synthesis
87   includes precipitation, microemulsions, hydrothermal/solvothermal, sol-gel, electrochemical
88   deposition, chemical bath deposition, and so on. There are several excellent reviews describing the
89   synthesis of ZnO nanostructures [6-9]. In this paper, we mainly focus on ZnO hierarchical
90   nanostructures synthesized by different solution phase methods.

91   *2.1. Precipitation*

92   In a typical precipitation process, different kinds of alkalis (NaOH, KOH, ammonium, urea,
93   hexamethylene tetramine (HMT), etc) and zinc sources (zinc salts, zinc foil, etc) are involved in the
94   reaction system (Figure 3a). A resultant precipitate is collected by filtration or centrifugation. The
95   morphology and assembly of the ZnO products can be controlled by adjusting the reaction
96   conditions, including the concentration of reacted solutions, temperature, time, and additives to
97   tune the reaction steps. Sepulveda-Guzman et al. [10] synthesized ubmicron ZnO arrays by a simple
98   one-step aqueous precipitation method with zinc nitrate ($Zn(NO_3)_2$) and sodium hydroxide (NaOH)
99   as the reagents. The effect of reaction temperature on the morphology change was studied.
100 Snowflake-like and flower-like morphologies were obtained at 60 ^{o}C and 70 ^{o}C. The ZnO arrays are
101 formed through self-aggregation process, and that such an oriented aggregation is enhanced by
102 increasing the reaction temperature. In another work, Oliveira and co-workers [11] systematically
103 investigated the influence of zinc salts ($Zn(NO_3)_2\cdot6H_2O$, zinc sulfate ($ZnSO_4\cdot7H_2O$)), pH value,
104 temperature, additives (sodium sulfate, sodium dodecyl sulfate) on the final ZnO morphology and
105 size. The results show the importance of nucleation of nanometric primary particles followed by
106 oriented aggregation to produce uniform submicrometric particles.
107   It should be noted that ZnO is a typical amphoteric oxide, which can be etched in either acid or
108 alkali environment. The reaction between the zinc ions and alkaline ions results in the formation of
109 ZnO crystals. Meanwhile, the newly formed ZnO further reacts with alkaline until an equilibrium is
110 achieved. Thus, tuning the precipitation (growth) and in-situ etching provides a facile approach to
111 control the morphology of nanocrystals [12-14]. For example, Xi et al. [12] fabricated large-scale
112 arrays of highly oriented single-crystal ZnO nanotubes by an in-situ chemical etching of the ZnO
113 nanorods. Yang et al. have demonstrated a novel anisotropic etching methodology for the synthesis
114 of complex Ag nanoparticles shapes by controlling the concentrations of etching solution, and
115 highlighted their important applications as highly sensitive surface enhanced Raman spectroscopy
116 substrates [13]. In our previous studies [4], we reported a simple precipitation to synthesize ZnO 3D
117 hierarchical structures by using $Zn(NO_3)_2\cdot6H_2O$, Zn foil, and KOH as the zinc souce and alkalis.
118 Importantly, the morphology of the hierarchical structures can be simply selected by changing the
119 KOH concentrations. The morphology of the products are sheet, flower-like microsphere assembled
120 by nanosheets, flower-like microsphere assembled by nanoneedles, and flower-like microsphere
121 assembled by thinner nanoneedles when the concentration of KOH increased from 0.5 to 2, 4, and 8
122 M, respectively (Figure 4a). A possible formation mechanism based on preferential etching of KOH
123 along the [001] direction of ZnO sheets was proposed (Fig. 3a-III). The growth or/and etching can be

124 further controlled by adding suitable capping agents that prefer to absorb on specific crystal planes,
125 making it possible to fine control over the morphology. Tian et al. [15] demonstrated that citrate
126 ions can selectively adsorb on the (001) surfaces of ZnO crystals and thus inhibit the growth along
127 <001> orientations. Based on these knowledge, they synthesized large arrays of oriented ZnO
128 nanorods with controlled aspect ratios and a series of complex morphologies. In our studies, we
129 combined the selective capping (citrate ions) and etching (KOH) together to capture the
130 intermediate of the morphology change, and proposed a possible formation mechanism based on
131 capping–etching competitive interactions (Figure 4b) [16]. The strategy can also be applicable to the
132 synthesis and modification of other materials by careful selecting suitable capping agents and
133 etchants.

134

135

Figure 3. Typical solution phase methods for the synthesis of 3D ZnO hierarchical nanostructures. (a)
precipitation, (b) microemulsions, (c) hydrothermal/solvothermal, (d) sol-gel, (e) electrochemical
deposition, and (f) chemical bath deposition.

139
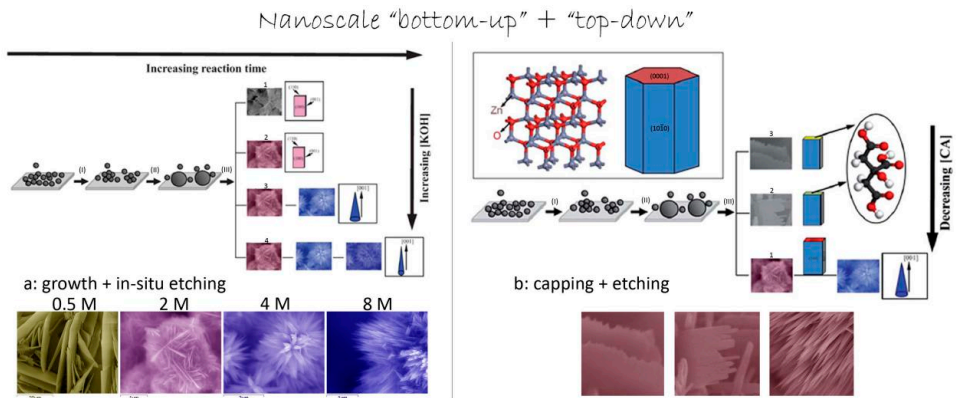
Figure 4. Schematic illustration of the formation process of ZnO 3D hierarchical structures via the
combining of (a) growth and in-situ etching (reprinted from [4] with permission, Copyright The
Royal Society of Chemistry, 2012); (b) capping and etching (reprinted from [16] with permission,
Copyright The Royal Society of Chemistry, 2015).

144

145   *2.2. Microemulsions*

146   Materials synthesis via microemulsion is occurred in a stable mixed solution that contains
147   water, oil, and surfactant. Depending on the properties of immiscible liquid-liquid interface, the
148   formation of microemulsion can be in the form of oil-swollen micelles dispersed in water
149   (oil-in-water, or O/W) or the reverse case, i.e. water swollen micelles dispersed in oil (water-in-oil,
150   W/O) (Figure 3b). The two configurations are usually named as microemulsion and reverse
151   microemulsion, respectively [17]. The typical size of the microemulsion or reverse microemulsion is
152   samller than 100 nm, therefore, the microemulsions can be used as nanoreactors for materials
153   synthesis, which provides a bottom-up route to control the size and morphology by adjusting the
154   microemulsion properties. By studying the phase diagrams of oil-water-surfactant system
155   containing toluene, zinc acetate solution, cetyltrimethylammonium bromide and butanol, Lin et al.
156   obtained the desired size and shape of ZnO particles [18]. This study demonstrates the importance
157   of investigating the the intrinsic properties of this multi-liquid-phase system.

158   *2.3. Hydrothermal and Solvothermal*

159   Hydrothermal synthesis is referred to the materials synthesis by chemical reactions of
160   substances in a sealed heated aqueous solution above ambient temperature and pressure, while
161   solvothermal is very similar to the hydrothermal route except the precursor solution is usually
162   non-aqueous (Figure 3c) [19-21]. Well control over the hydrothermal/solvothermal synthetic
163   conditions is a key to the synthesis of ZnO nanomaterials with defined structure, morphology,
164   composition, and assembly. Typical control experimental parameters include reagents, solvent,
165   additives, filling degree, temperature, time, and so on [22, 23]. In addition, substrate is an important
166   and interesting parameter that can affect the ZnO morphology, especially the aligned ZnO
167   nanostructures. In a study, ZnO nanostructures on Zn foil was synthesized by hydrothermal
168   synthesis [24]. The morphology and assembly of ZnO arrays are dependent on the solvent
169   properties. Specifically, ZnO nanorod arrays and randomly scattered nanorods are obtained in the
170   mixed solvent containing ammonia aqueous solution (1%) and pure water, and pure water system,
171   respectively. Moreover, repetitive hydrothermal or solvothermal treatment can yield more complex
172   and hierarchical configurations. By employing this simple strategy, Ko et al. [25] synthesized high
173   density and long branched tree-like ZnO nanoforests. In a report of Joo et al. [26], single-crystalline
174   ZnO nanowires were grown on substrates with zinc oxide seed layers in aqueous solutions by
175   hydrothermal method. The effect of specific additives on the ZnO morphology was studied in detail.
176   The results show that the addition of positively charged complex ions (Cd, Cu, Mg, Ca) and
177   negatively charged complexes (Al, In, Ga) promote low and high aspect ratio growth of ZnO
178   nanostructures. They demonstrated that face-selective electrostatic crystal growth inhibition
179   mechanism governed this selective synthesis.

180   *2.4. Sol-Gel Processing*

181   The sol-gel process contains the formation of solid material from a solution by using a sol or a
182   gel as an intermediate step. The synthesis of metal oxide materials often involves controlled
183   hydrolysis and condensation of the alkoxide precursors or salts. Figure 3d illustrates the main steps
184   of preparation of metal oxides powder by the sol-gel process: (i) preparation of the precursor
185   solution; (ii) hydrolysis of the molecular precursor and polymerization via successive bimolecular
186   additions of ions, forming oxo-, hydroxyl, or aquabridges; (iii) condensation by dehydration; (iv)
187   solvent evaporation and organic compounds removal to form xerogel; and (v) heat treatment of the
188   xerogel to form powers. Properties of the final products, including the particle size, surface area,
189   crystallinity, and agglomeration, are highly dependent on the reactiuon parameters, especially the
190   precursors, solvents, additives, evaporation, drying, and post-treatment conditions [27]. Tseng et al.
191   [28] employed the sol-gel process to synthesize ZnO polycrystalline nanostructures using
192    $Zn(CH_3COO)_2 \cdot 2H_2O$ as the zinc solute and different alcohols as solvents (glycol, glycerol, and
193   diethylene glycol). The morphology of the final ZnO were fiber, rhombic flakes, and spherical

194 particles. The formation of thorn like ZnO nanostructures in sol-gel process was reported by Khan
195 and co-workers [29]. They further modified this method by mechanical stirring during the sol
196 generation, and found the agitation speed was a critical value in determining the size, aspect ratio
197 of the particles. Higher stirring speed is favorable for anisotropic growth of ZnO nanoparticles.

198 *2.5. Electrochemical and Chemical Bath Deposition*

199 Electrochemical deposition (ECD) and chemical bath deposition (CBD) methods are facile and
200 can produce materials or nanostructures that cannot be obtained by other deposition methods. CBD
201 process only requires suitable solution containers and substrate mounting devices (Figure 3e), while
202 for ECD method, additional power supplies, electrodes (counter electrode/CE, reference
203 electrode/RE) are necessary, and the substrate (working electrode/WE)must be conductive (Figure
204 3f). More importantly, the morphology and orientation of the deposited samples can be tuned by
205 controlling the reaction thermodynamics and kinetics, including solution properties, additives,
206 substrate, temperature, and electrochemical parameters (applied potential, current density, etc)
207 [30-35].
208 The synthesis of ZnO nanostructures via ECD process includes the reduction of precursor at
209 the electrode, the supersaturation at the vicinity of the electrode, and subsequent precipitation.
210 Theoretically, factors that affect any step should be considered to achieve the well control of final
211 structures. In this regard, Illy et al. [36] systematically studied the effect of various experimental
212 parameters (electrolyte concentration, pH value, reaction temperature, and overpotential) on the
213 morphology, thickness, transparency, roughness and crystallographic orientation of the ZnO
214 materials. They found that ZnO nanostructures with (002) preferential orientation and controlled
215 thickness can be grown by using optimized parameters, which are important for organic
216 photovoltaic applications. Different additives can either interact with the ions in the electrolyte,
217 absorb on specific sites on the deposited ZnO structure, or change the electrolyte itself (conductivity,
218 viscosity, etc), resulting in a different deposition pathways and thus final products. In a study by
219 Oekermann and co-workers [37], the addition of water soluble tetrasulfonated
220 metallophthalocyanines (TSPcMt), in which Mt = Zn(II), Al(III)[OH] or Si(IV)[OH], in the electrolyte
221 containing zinc nitrate yields completely different morphology and assembly, which is ascribed to
222 the preferential adsorption of the additive molecules onto the crystal planes of ZnO. The
223 morphology and assembly of the depositions can also be controlled by substrate, for example
224 patterned or flexible ZnO hierarchical nanostructures can be obtained by applying corresponding
225 substrates [38].
226 Synthesis of ZnO nanostructures via CBD is based on a direct chemical reaction involving
227 dissolved zinc ions and oxygen precursors in the solution. Different from ECD where the
228 deposition only occurs on the conductive substrate, the growth of ZnO in CBD process can take
229 place either in the solution or on the substrate surface. The morphology and assembly of ZnO
230 products can also be controlled by the solution, additives, substrate, and so on [39].
231 The above discussed different solution phase synthesis methods can be combined together or
232 with other treatments, such as microwave heating, sonochemistry, etc, to achieve even more
233 complex and useful hierarchical nanostructures with useful applications. For example, sol-gel
234 processing or microemulsions is often employed with hydrothermal/solvothermal treatment to
235 prepare various nanostructures [40]. The pre-synthesized ZnO nanostructures via hydrothermal or
236 ECD methods can be further etched to form needle or tube arrays [41]. The assembly of ZnO
237 architectures can be tuned by means of ECD via deformation and coalescence of soft colloidal
238 templates in reverse microemulsion [42]. In a word, solution phase synthesis provides plenty of
239 room to control and optimize hierarchical ZnO architectures for diverse applications.
240

241 **3. Applications of 3D ZnO Hierarchical Nanostructures**

242 3D ZnO hierarchical nanostructures show unique advantages of high surface area, porous
243 structures, and synergistic interactions of the constituted nano building blocks. Therefore, 3D ZnO

nanostructures possess improved physical/chemical properties, such as enhanced light harvesting, increased reaction sites, and improved electron and ion transportation, which are highly needed for optical, electrical, and electrochemical applications. In this paper, we will review the most recent progress in the research activities on 3D ZnO hierarchical nanostructures used for photocatalysis, field emission, electrochemical sensors, and electrodes for lithium ion batteries.
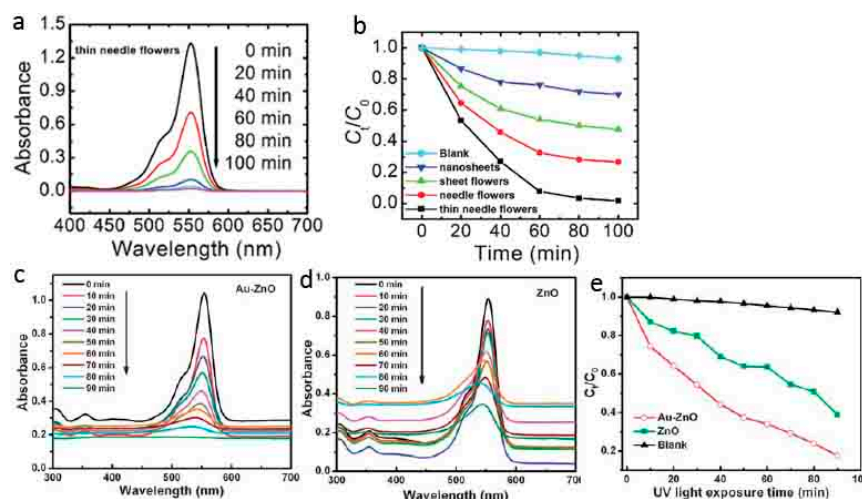
3.1. Photocatalysis

ZnO nanostructures have attracted much attention in the fields of photocatalysis, including photocatalytic degradation of organic contaminants, photocatalytic water splitting, and so on, due to the notable merits such as nontoxicity, biological compatibility, and universality. Typical steps involved in heterogeneous photocatalysis process are as follows (Figure 5) [43]: (1) light absorption; (2) the generation and separation of photoexcited electrons and holes; (3) the migration, transport and recombination of carriers; and (4) surface electrocatalytic reduction and oxidation reactions. The overall catalysis efficiency is related to the cumulative effects of these consecutive steps. For ZnO photocatalysts, the activity is limited by the intrinsic wide bandgap (3.0-3.2 eV) and the high electron-hole recombination rate, which can be tuned by optimizing the structural parameters of the photocatalysts, such as size, morphology, assembly, specific surface area, and the defect density [44]. Compared to the 0D, 1D, or 2D counterparts, 3D ZnO hierarchical nanostructures show advantages of high surface area and porous structures, enhanced light harvesting, and synergistic effects between the nano building blocks. All these characters are beneficial for the photocatalysis enhancement.
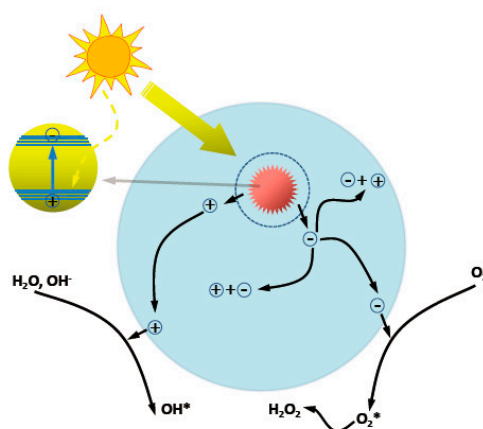
Figure 5. Schematic illustration on the photocatalytic processes in ZnO (reprinted and modified from [43] with permission, Copyright Continental Press, 2016).

The comparison of the photodegradation of organic dye Rhodamine B (RhB) under UV-irradiation with different 3D ZnO hierarchical nanostructures yielded by facile solution phase method is shown in (Figure 6a, b) [4]. Under the same experimental conditions, the relative photocatalytic activity is thin needle flowers > needle flowers > sheet flowers > nanosheets. The significant improvement in the photocatalytic activity of the thin needle flowers structure can be attributed to the following reasons: (1) optical quality and special structural features; (2) the large active surface area and interspaces of the flower structure, which facilitate the diffusion and mass transportation of RhB molecules and hydroxyl radicals; (3) the improved efficiency of electron–hole separation. The morphology of ZnO nanostructures dependent photocatalysis is later demonstrated in the degradation of methylene blue in aqueous solution [45]. By coupling the strategies of elemental doping [46], defect engineering [47], modifying the surface with visible light active materials [48] or plasmonic-metal nanostructures (Ag, Pt, Au, etc) [49], the photodegradation properties of 3D ZnO hierarchical nanostructures can be further improved. For example, we

281 evaluated photocatalytic performance of ZnO needle flowers and Au nanoparticles/ZnO needle
282 flowers composite (Au/ZnO) by degradating organic dye RhB under UV irradiation (Figure 6c-e)
283 [50]. The pure ZnO showed observable photocatalytic activity but with rather slow kinetics. Only
284 ~60% of the RhB was decomposed within 90 min. In contrast, when the Au/ZnO composites were
285 applied as the photocatalyst, a significant synergistic enhancement effect was observed, i.e., RhB was
286 decomposed thoroughly within 90 min. The Au nanoparticles enhanced photodegradation is also
287 observed in ZnO sheet flowers. In these studies, besides the hierarchical morphology of ZnO
288 nanostructures, the improvement of photocatalytic properties can be ascribed to the presence of
289 noble metal nanoparticles. (1) The light absorption is increased due to the strong surface plasmon
290 resonance of the noble metal nanoparticles; (2) the efficiency of charge separation of the
291 photo-generated electron-hole pairs is increased due to the strong electronic interaction between
292 strong electronic interaction and ZnO.
293

295 **Figure 6.** Photocatalytic degradation of RhB via (a, b) 3D ZnO hierarchical nanostructures with
296 different morphologies (reprinted from [4] with permission, Copyright The Royal Society of
297 Chemistry, 2012); (c-d) ZnO needle flowers and Au nanoparticles/ZnO needle flowers composite
298 (reprinted from [50] with permission, Copyright The Royal Society of Chemistry, 2011).

299 The above routes to improve the degradation properties in ZnO hierarchical photocatalysts can
300 also be applied to photosplit water to generate hydrogen. For example, elemental doping and defect
301 engineering are effective to narrow the bandgap of ZnO materials, which results in an extension of
302 light absorption range from UV into visible light range, while generating interface structures by
303 depositing plasmonic noble metals separates photogenerated carriers, improves visible and
304 near-infrared photo-absorption, and thus achieves high-performance photocatalytic hydrogen
305 evolution.

306 *3.2. Field Emission*

307 Field emission devices show several advantages, such as the resistance to temperature
308 fluctuation and radiation, less power consumption, low thermionic noise, low energy spread,
309 miniature volume and nonlinear, exponential current–voltage (I-V) relationship in which a small
310 variation in the voltage results in a large change in the emission current instantaneously [51].
311 Theoretical calculations show that the external filed induces a decrease of the surface barrier height
312 by a value of $\Delta\Phi \sim 3.8\ F^{1/2}$ (for Φ in eV and F in V/Å) (Figure 7a), and the field is off the order of $\sim10^9$
313 V/m. If the emitter surface is sharp configuration as shown in Figure 7b, electrons can be extracted at
314 a considerably lower applied field. The relationship between the field emission current density (J)
315 and the applied electric field (E) is described by Fowler-Nordheim (FN) equation:
316 $J = \left(A\beta^2 E^2/\Phi\right)\exp\left[-B\Phi^{3/2}(\beta E)^{-1}\right]$, where A ($1.54 \times 10^{-6}$ A eV V^{-2}) and B (6.83×10^3 eV$^{-3/2}$ V μm^{-1}) are the first

317 and second F-N constants, Φ is the work function, and β is the field enhancement factor, which
318 reflects the the magnitude of electric field at the emitting surface. The emission current density at a
319 constant cathode-anode distance is strongly dependent on the work function Φ and the field
320 enhancement factor β that is related to geometric configuration of the emitter, crystal structure,
321 conductivity, and so on.
322
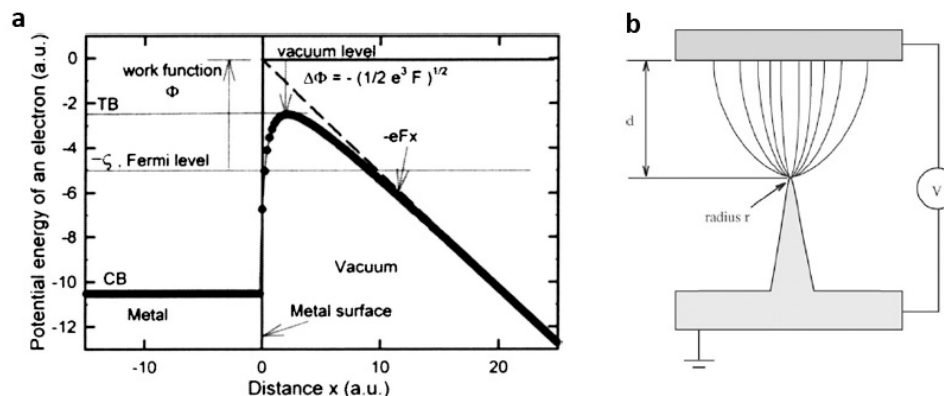
324 **Figure 7.** (a) Potential energy of an electron near the cathode surface (reprinted from [52] with
325 permission, Copyright American Vacuum Society, 2007); (b) Illustration of field electron emission
326 from a tip (reprinted from [53] with permission, Copyright Elsevier B.V., 2004).

327 With inherent properties of thermally stable and oxidation resistant, ZnO nanostructures show
328 potential to be a good candidate for field emission. Moreover, a variety of ZnO nanostructures can
329 be synthesized by facile solution phase methods as discussed above, which not only reduce the cost,
330 but also make it possible to fabricate flexible field emission devices based on polymer or other metal
331 substrate materials [54, 55].
332 Field emission studies on ZnO nanorod arrays synthesized on zinc foils by the solvothermal
333 route are presented by Dev et al [56]. The effect of solvothermal parameters including the solvent
334 (distilled water and ethylenediamine), temperature, and time on the morphology and field emission
335 properties of ZnO nanostructures are studied. It was observed that with the increase in
336 ethylenediamine concentrations the alignment of the nanorods gets better, corresponding to the
337 increasement of field enhancement factor from 850 to 1044. ZnO nanotube arrays were prepared by
338 hydrothermal reaction in ammonia and zinc chloride solutions by Wei et al [57]. The turn-on field of
339 the ZnO nanotube arrays was extrapolated to be about 7.0 Vm^{-1} at a current density of 0.1 Acm^{-2}, the
340 emission current densities reached 1 mAcm^{-2} at a bias field of 17.8 Vm^{-1}, and the field enhancement
341 factor was estimated to be 910. Cao et al. [58] reported the field emission of wafer-scale ZnO
342 nanoneedle arrays synthesized by template-free electrochemical deposition method. The field
343 enhancement factor of the ZnO nanoneedle arrays was 657 with a working distance of 250 μm
344 between the cathode and anode. In our studies [59], we compared the field emission properties of
345 ZnO nanowire arrays with flat ends and nanoneedle arrays with sharp ends (Figure 8a). The ZnO
346 nanowires were synthesized by hydrothermal method at 70 $^{\circ}$C. Then solution etching was employed
347 to form ZnO nanoneedles at room temperature. The turn-on electronic fields of ZnO nanoneedles
348 and nanowires are 2.7 and 5.3 V μm^{-1} at a current density of 10 μA cm^{-2}. The threshold electronic
349 fields, which defined as the field value at the emission current density J of 0.1 mA cm^{-2}, of ZnO
350 nanoneedles and nanowires are 3.9 and 6.1 V μm^{-1}, respectively (Figure 8b). The field enhancement
351 factors were estimated to be 4939.3 for ZnO nanoneedles and 1423.6 for ZnO nanowires (Figure 8c).
352 In addition, there is no obvious degradation of the current density, demonstrating the excellent
353 emission stability of the ZnO array materials (Figure 8d). This study highlights the important effect
354 of emitter geometry on the field emission.
355
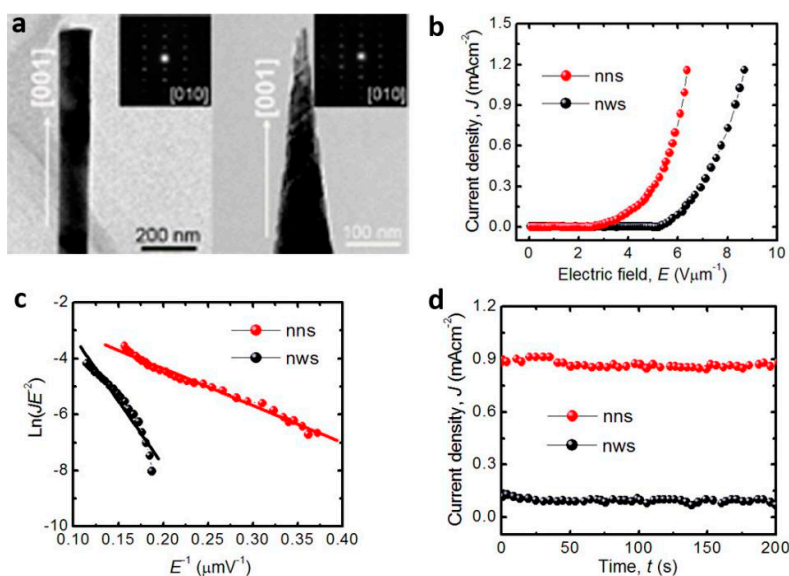
Figure 8. The comparison of field emission properties of ZnO nanowires with flat ends and nanoneedles with sharp ends. (a) TEM images; (b) J-E curves; (c) FN plots; (d) stability of the emission current density under a constant electric field of 6.0 Vμm^{-1} (reprinted from [59] with permission, Copyright Elsevier B.V., 2017).

Besides sample geometry, intrinsic electric conductivity in ZnO material also influences the field emission properties. Using a simple solution reduction method, oxygen-deficient ZnO nanorod arrays were synthesized by Su et al [60]. The concentration of oxygen vacancies can be effectively controlled by adjusting the reduction temperature ranging from 30 -110 ^{o}C, resulting in a controlled tailoring of the band structure of the ZnO. The final oxygen-deficient ZnO nanorod arrays with optimized topography show excellent field emission properties, the threshold electronic field was as low as 0.67 Vμm^{-1}, the field enhancement factor was as large as 64601, the stability was also favorable. In addition, doping with metal [61] or non-metal elements [62] through facile solution phase methods is also an effective method to improve the field emission properties of ZnO nanostructures. Doping induced conductivity enhancement and electron increasement in the conduction band are the possible reasons for the emission properties improvement.

3.3. Electrochemical Sensors

Continuous monitoring biological molecules and metal ions has attracted much interest due to the significant use in biotechnology, medicines, food and processing industry, and as a valuable biological marker for many oxidative biological reactions. In this regard, electrochemical sensors show unique advantages of high sensitivity, wide range of detection, real-time monitoring, ease of fabrication and control, reproducibility, and low cost, which can not be simultaneously achieved by other techniques, such as radioisotope tracing and nuclear magnetic resonance. The principle of electrochemical sensors is based on electroanalytical chemistry techniques in which quantitative investigating sensing is made by varying the potential and measuring the resulting current as an analyte reacts electrochemically with the working electrodes surface (nanostructures modified glass carbon electrode/GCE, Figure 9). The frequently used electrochemical techniques employed in sensors include cyclic voltammetry (CV), linear scan voltammograms (LSV), differential pulse voltammetry (DPV), electrochemical impedance spectroscopy (EIS), and so on.

Thanks to the biocompatible and nontoxic nature and high sensitivity to chemical species, ZnO nanostructures have been intensively studied as different kinds of electrochemical sensors to monitor important biological molecules and metal ions in organism, typically include glucose, dopamine, uric acid, L-lactic acid, L-Cysteine, hydrogen peroxide, potassium, sodium, calcium, magnesium, and iron ions. Due to the large surface area and porous nature, 3D ZnO hierarchical

390 nanostructures based electrochemical sensors generally show good sensitivity, low detection limit,
391 long-term stability, and repeatability.
392

393
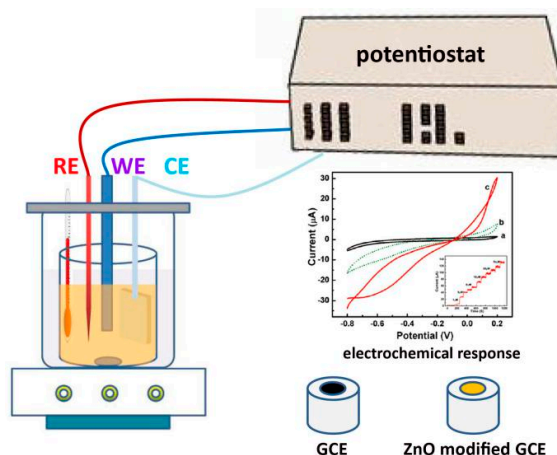
394   **Figure 9.** Schematic illustration of the electrochemical sensor testing.

395   Yang et al. [63] prepared ordered single-crystal ZnO nanotube arrays on indium-doped tin
396 oxide coated glass by combining electrochemical deposition and subsequent chemical etching
397 methods. The samples were used as a working electrode to fabricate an enzyme-based glucose
398 biosensor, which exhibited high sensitivity of 30.85 μA cm^{-2} mM^{-1} at an applied potential of + 0.8 V
399 vs. SCE, wide linear calibration ranges from 10 μM to 4.2 mM, and a low limit of detection at 10 μM
400 for sensing of glucose. We studied electrochemical sensing of hydrogen peroxide by using noble
401 metal nanoparticle-functionalized ZnO nanoflowers. Firstly, the hierarchical flower-like ZnO
402 structures were synthesized by a co-precipitation method in a solution containing Zn (NO$_3$)$_2$·6H$_2$O
403 and KOH. Au or Ag nanoparticles were decorated on the surface of ZnO nanoflowers by subsequent
404 hydrothermal treatment. Au/ZnO, Ag/ZnO and bare ZnO nanostructures modified GCE were
405 fabricated and used as H$_2$O$_2$ sensors. The electrodes were tested in 0.05 M Phosphate buffered saline
406 at pH = 7.2 with a platinum counter electrode and a saturated calomel electrode (SCE) reference
407 electrode. CV results show that the electrochemical oxidation of H$_2$O$_2$ started at about -0.68 to -0.1 V
408 versus SCE (Figure 10a), and the CV response for Ag/ZnO electrode was much higher than Au/ZnO
409 and bars ZnO electrodes. In addition, the Ag/ZnO electrode also exhibited rapid and sensitive
410 response to the change in concentration of H$_2$O$_2$ and the amperometric current is noticeably
411 increased upon successive addition of H$_2$O$_2$ (Figure 10b). The linear range of calibration curve for
412 these modified electrodes was from 1 to 20 μM (correction factor, R = -0.998) with a low limit of
413 detection (LOD) of about -2.5 μM (Figure 10c). The sensitivity of the H$_2$O$_2$ sensor for Ag/ZnO
414 modified electrode is 50.8 μA cm^{-2} μM^{-1}, which is much higher than that of Au/ZnO and bare ZnO
415 electrodes. Stability test showed that Ag/ZnO modified electrode was more stable as compared to
416 Au/ZnO and bare ZnO showing higher value of current with steady state current loss of 1.5 % after
417 300 s (Figure 10d). This work demonstrated that noble metal-integrated ZnO nanostructures
418 provided a new platform for applications in designing enzymeless biosensors. By decorating ZnO
419 nanostructures with optimized alloy clusters, the electrochemical activity can be further improved
420 [64].
421   Due to the mild condition of solution phase synthesis, ZnO nanostructures can be directly grew
422 on a wide range of flexible and conductive substrates, making it possible to fabricate free-standing
423 and flexible electrochemical sensors. For example, ZnO nanorods were uniformly anchored on the
424 surface of carbon cloth directly by a simple hydrothermal method [65]. The products were directly
425 used a electrode for the simultaneous determination of dihydroxybenzene isomers. The electrodes
426 showed good electrochemical stability, high sensitivity, and high selectivity. The linear ranges of
427 concentration for hydroquinone, catechol, and resorcinol were 2–30, 2–45, and 2–385 μM,
428 respectively, and the corresponding limits of detection (S/N = 3) were 0.57, 0.81, and 7.2 μM.

429

430
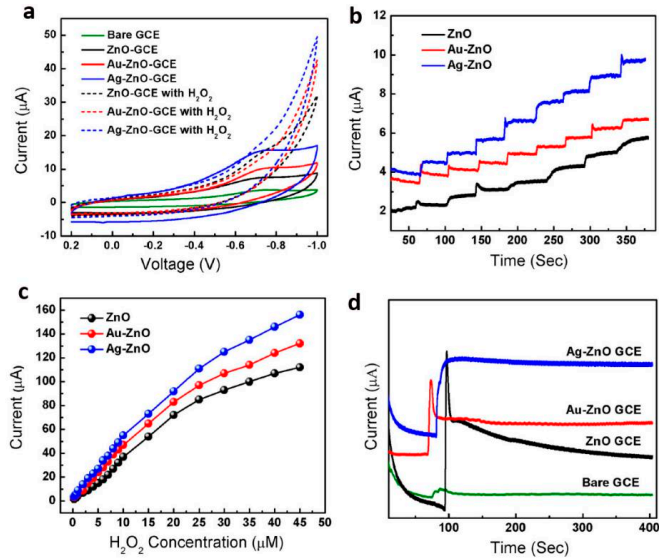
431 **Figure 10.** (a) Cyclic voltammograms of bare and modified GCE with pure ZnO, Au/ZnO, and
432 Ag/ZnO in the absence of H_2O_2 and in the presence of H_2O_2; (b) amperometric response of three
433 modified GCE at constant voltage of -0.45 V with successive addition of 1 μM H_2O_2 in 0.05 M PBS
434 under stirring; (c) corresponding calibration curves of the three modified electrodes and (d) stability
435 plot of the three modified GCE at constant potential of -0.45 V in the presence of 1 μM H_2O_2
436 (reprinted from [66] with permission, Copyright Springer Science+Business Media Dordrecht, 2016).

437 *3.4. Lithium Ion Batteries*

438   With a growing world population and increasing industrialization, energy and environment
439 become the two main factors that restrict the society sustainability. It is thus of urgent need to
440 develop renewable energy conversion and storage techniques. Lithium ion batteries are one of the
441 most important energy storage devices, which dominate the market of portable electronic devices,
442 and also show potential in hybrid/electric vehicles. Typical lithium ion batteries system mainly
443 includes anode, cathode, electrolyte, and separator, of which active materials used in both electrodes
444 play pivotal roles in determining the overall performance of batteries. For example, the specific
445 capacity of graphite anode in current commercial lithium ion batteries is as low as 372 mAhg^{-1},
446 which is insufficient for many applications. Searching for high-performance electrode materials
447 remains one of the most important focus in battery community. Among many potential electrode
448 candidates, ZnO nanostructures have attracted much attention due to the abundance of raw
449 materials, environmental benignity as well as facile synthesis [67-71]. In principle, the reaction
450 between lithium and ZnO anodes is occurred through the so-called mechanism of "conversion
451 reaction". During lithiation, ZnO anode undergoes a conversion reaction to form Li_2O embedded
452 with nanosized metallic zinc clusters. This step is followed by an alloying reaction between lithium
453 and the formed Zn NPs. The reaction processes are described as the following equations: $ZnO + 2Li^+$
454 $+ 2e^-$ $Zn + Li_2O$ (conversion step); $Zn + Li^+ + e^-$ $LiZn$ (alloying step), which yields a higher
455 theoretical capacity (987 mAhg^{-1}) than that of graphite [72-74].
456   However, the practical using of ZnO based anodes mainly suffer from low Columbic efficiency
457 (especially in the first cycle), severe capacity fading, and poor electrochemical kinetics [75,76]. Firstly,
458 the conversion step in the lithiation reaction represents the largely irreversible reduction process of
459 ZnO to metallic Zn. This irreversible chemical transformation is partly responsible for the large
460 initial irreversible capacity loss. Secondly, the alloying step is accompanied by a large volume
461 change (~228%) upon cycling, which results in material pulverization, electrode failure, and thus
462 rapid capacity fading. The volume change of the anodes also results in the formation of unstable
463 solid-electrolyte interphase (SEI) layer, which continuously traps Li ions leading to capacity loss.

Thirdly, the low intrinsic electronic conductivity of ZnO materials causes moderate lithium ion diffusion coefficient and limits the high-rate applications. To enhance the lithium storage properties of ZnO anodes, the construction of 3D ZnO hierarchical nanostructures with proper morphology, composition, and assembly has been proven to be an effective approach to overcome the above limitations. (1) Capacity. Compared to the corresponding nanobuilding blocks, hierarchical structures possess larger surface area, which increases the contact area between electrode and electrolyte and thus the number of active sites for electrode reactions with lithium ions. In addition, the hierarchical electrodes can lead to new lithium storage mechanisms, such as surface, interface, and nanopore storage, which lead to excess capacity. (2) Stability. The low dimensional ZnO nanobuilding blocks have high mechanical strength, more resistance to mechanical damage, and can be engineered to allow volume change, and the assembled hierarchical structures can also prevent the possible agglomeration during the continuous cycling. Both are essential to ensure the structural integrity of the electrodes and long term stability. (3) Rate performance. The rate of battery operation is related to the solid-state diffusion of lithium ions in the electrodes, which can be reduced in the nanoscale electrodes.

The assembly of ZnO hierarchical nanostructures show great influence on the battery performance. Zhang et al [77]. synthesized ZnO nanostructures with different morphology by a facile hydrothermal and subsequent annealing treatment. The ZnO particles anode delivers the largest initial discharge capacity of 1815.8 mAhg^{-1}, and a reversible charge capacity of 870.0 mAhg^{-1} at the current density of 50 mAg^{-1}, while cabbage-like ZnO nanosheets electrode displays better cycling stability. In other work, ZnO nanorod arrays with dandelion-like morphology were grown on copper substrates by a hydrothermal synthesis method [66]. The samples can be directly used as electrodes without any additives or binders. Cycling performance was performed at a current density of 0.1 mAcm^{-2}. The charge capacity of the dandelion-like ZnO electrode decreases to 596, 481 and 419 mAhg^{-1} in the second, third and fifth cycle, respectively. The ZnO arrays keep a capacity larger than 310 mAhg^{-1} even after 40 cycles, which is about 4 times higher than the stabilized capacity of the bulk ZnO electrode. The unique dandelion-like binary-structure played an important role in the electrochemical performance of the array electrodes.

Besides the architecture design, the electrochemical properties of ZnO anodes can further be improved by composting with an electronically conductive agents (such as carbon nanofibers, carbon nanotubes, graphene, metals, metal compounds and so on) [78-80]. Those additives can not only enhance the conductivity of the electrodes but also modify the chemistry at the electrode/electrolyte interface. Therefore, 3D ZnO hierarchical nanostructures with suitable surface or interface composition modification show unique advantageous as improved lithium storage properties. In our previous studies, we synthesized hierarchical flower-like ZnO nanostructure by a facile solution phase approach. Au nanoparticles were functionalized on the surface of ZnO by subsequent electrochemical deposition treatment. The diameter of the pristine ZnO microflower is about 6-10 μm, and the length of an individual nanoneedle varies by 2-3 μm (Figure 11a). After electrodeposition, Au nanoparticles with an average diameter of 4-6 nm are decorated on the surface of each ZnO nanoneedle (Figure 11b,c). Comparing to the bare ZnO material, the Au-ZnO hybrid hierarchical structures possess large specific surface area, abundant void spaces, stable structure and strong electronic interaction between Au nanoparticles and ZnO. Those structural characters are beneficial for lithium storage enhancement. The initial discharge and charge capacity of Au-ZnO electrode are 1280 and 660 mAhg^{-1}, respectively, yielding a Coulombic efficiency of 79% (Figure 11d). In comparison, the initial discharge and charge capacity of pure ZnO electrode are 958 and 590 mAhg^{-1}, respectively (Figure 11e). The initial Coulombic efficiency of ZnO electrode is 52%, which is 27% lower than that of the Au–ZnO hybrids electrode. The stability test results show that the charge capacity of the Au–ZnO electrode decreases to 519 and 485 mAhg^{-1} after the second and third cycle, and stabilizes at 392 mAhg^{-1} after 50 cycles (Figure 11f). In contrast, the capacity of the ZnO electrode decays rapidly to 252 mAhg^{-1} (Figure 11f). The better lithium storage properties, including improved capacity and cycle life of the Au–ZnO electrode can be attributed to the Au nanoparticles, which act as good electronic conductors and serve as good catalyst during lithiation/ delithiation process. Due

516   to the strong electronic interaction between Au nanoparticles and ZnO, electron can easily reach at
517   all the position where lithium ions intercalation takes place. This feature is very important when the
518   battery is cycled at high current density.
519

520
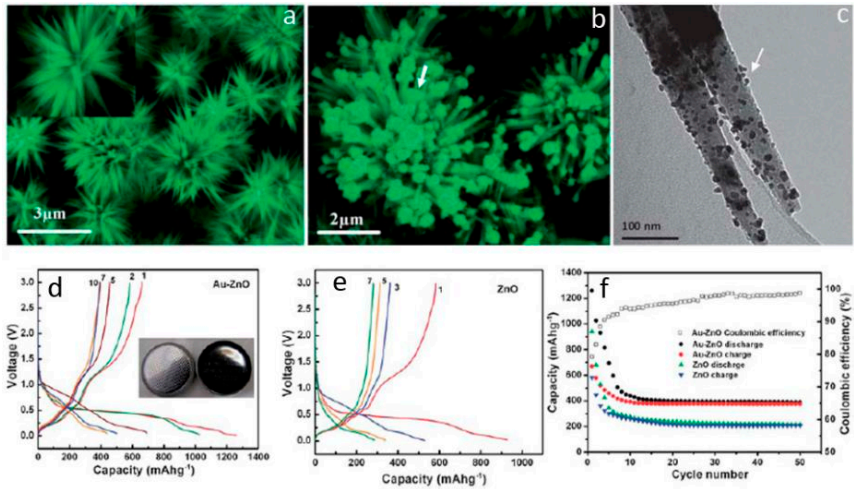
521   **Figure 11.** (a-c) Electron microscopy images and (d-f) lithium storage properties of the ZnO needle
522   flowers and Au nanoparticles/ZnO needle flowers composite (reprinted from [50] with permission,
523   Copyright The Royal Society of Chemistry, 2011).

524
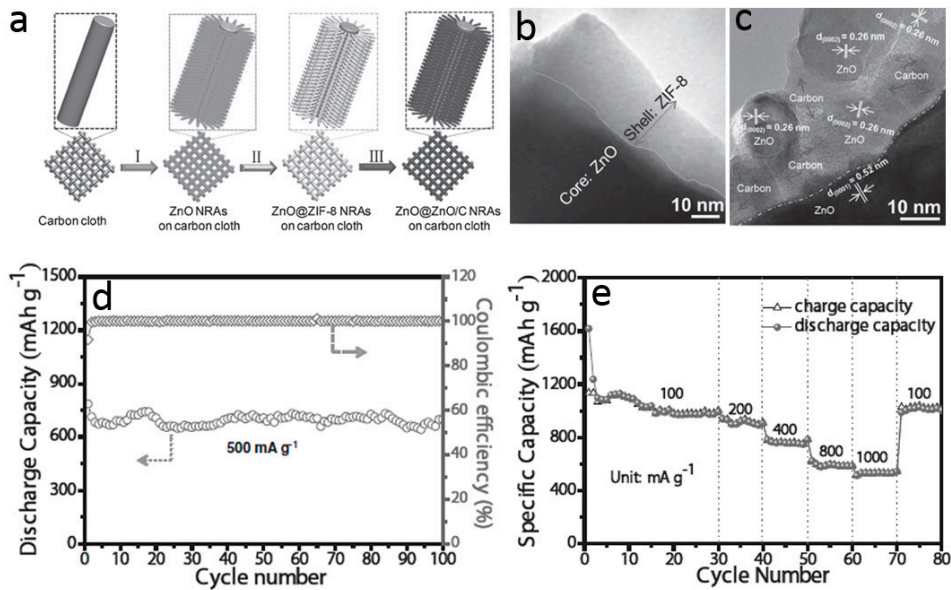
525   **Figure 12.** (a) Schematic illustrating the synthesis procedures of ZnO@ZnO QDs/C core-shell
526   nanorod arrays on carbon cloth; (b, c) TEM and HRTEM images; (d, e) lithium storage properties of
527   ZnO@ZnO QDs/C core-shell structures (reprinted from [84] with permission, Copyright
528   WILEY-VCH Verlag GmbH & Co. KGaA, Weinheim, 2015).

529   Anchoring ZnO nanostructures on various carbon materials, such as graphite, mesoporous
530   carbon, mesoporous carbon bubble, hierarchical porous carbon, vertically aligned graphene, and
531   graphene aerogels, also facilitates the electron and lithium ion transport during charge/discharge
532   cycles [81-83]. Those composite anodes show improved lithium storage properties, especially high
533   rate capacity, which are highly dependent on the strong interaction between ZnO and carbon
534   nanostructures. To strengthen this adhesion, one strategy is in-situ formation carbon modification
535   and ZnO nanostructures from metal organic compounds containing carbon and zinc elements. For

example, Zhang and co-workers designed a facile and scalable strategy to synthesize integrated, binder-free, and lightweight ZnO nanoarray-based electrode as shown in Figure 12a [84]. Firstly, aligned and ordered ZnO nanorods were grown on carbon cloth via low temperature solution deposition method. The ZnO nanorods were then served as the template as well as the Zn source to induce the formation of zeolitic imidazolate frameworks-8 (ZIF-8), a typical metal-organic framework, on the surface of ZnO nanorods (Figure 12b). Finally, unique ZnO@ZnO QDs/C core–shell nanorod arrays were obtained by thermal treatment in N_2. Structure studies show that the shell of each nanorod is constituted by amorphous carbon framework and ultrafine ZnO quantum dots (Figure 12c), resulting in a stronger adhesive force between carbon and the active ZnO materials, which is important to accelerate the charge transfer in the electrode. Benefit from this structure design, the resultant ZnO@ZnO QDs/C anode not only exhibits remarkable cycling performance (Figure 12d), but also provides a remarkable rate capability, i.e. a reversible capability of 1055, 913, 762, 591, and 530 mAhg^{-1} at the current density of 100, 200, 400, 800, and 1000 mAg^{-1} (Figure 12e).

It is worth mentioning that the ZnO nanostructures can also be used as anodes for sodium ion batteries [85,86], which are important complementarities of current lithium ion batteries. Due to the fact that sodium chemistry is similar with the case of lithium, the established electrode-design strategies for ZnO materials in lithium ion batteries system can be transferred to and expedite the sodium ion battery studies.

4. Conclusions and Perspective

Recent years witness explosive research and development efforts on ZnO materials, ranging from facile synthesis to advanced characterizations and device applications. 3D ZnO hierarchical nanomaterials possess high surface area with porous structures, facilitate multiple physical and chemical processes. In addition, the hierarchical materials not only inherit the excellent properties of an individual nanostructure but also generate new properties due to the interactions between the nano building blocks. Therefore 3D ZnO hierarchical nanostructures provide a wide range of applications. This review article summarized the main progress in the synthesis of 3D ZnO hierarchical nanostructures via different solution phase methods, such as precipitation, microemulsions, hydrothermal/solvothermal, sol-gel, electrochemical deposition, and chemical bath deposition. In each method, the synthesis principle, factors that affect the final structure and morphology, and typical examples are briefly discussed. Then the applications of the 3D hierarchical architectures in the fields of photocatalysis, field emission, electrochemical sensors, and lithium ion batteries are analyzed, especially the effect of hierarchical morphology on the performance are evaluated. Despite these impressive advances, several challenges still remain.

(1) Although great success has been made in the controllable synthesis of 3D ZnO hierarchical architectures, there is still room for improvement in terms of quality and scale of the products. Moreover, new synthesis methods also provide opportunities to explore novel morphology and understand the formation mechanism of the nanostructures.

(2) Besides the hierarchical architectures, the device performance is also related to the size, composition and defects of ZnO nanostructures. Coupling the 3D nanostructures with the ability of fine control over geometry and chemistry can further optimize the chemical and physical properties.

(3) Direct study the dynamic morphological and chemical evolution of ZnO nanostructures during the practical applications is of significance to study the performance degradation and develop strategies to improve the stability.

Conflicts of Interest: The authors declare no conflict of interest.

References

1. Sun, Y.; Chen, L.; Bao, Y.; Zhang, Y.; Wang, J.; Fu, M.; Wu, J.; Ye, D. The applications of morphology controlled ZnO in catalysis. *Catalysts* **2016**, *6*, 188/1-44.

585   2.   Baruah, S.; Dutta, J. Hydrothermal growth of ZnO nanostructures. *Sci. Technol. Adv. Mater.* **2009**, *10*,
586   013001/1-18.
587   3.   Burke-Govey, C. P.; Plank, N. O. V. Review of hydrothermal ZnO nanowires: Toward FET applications. *J.*
588   *Vac. Sci. Technol., B* 2013, 31, 06F101/1-12.
589   4.   Sun, H.; Yu, Y.; Luo, J.; Ahmad, M.; Zhu, J. Morphology-controlled synthesis of ZnO 3D hierarchical
590   structures and their photocatalytic performance. *CrystEngComm* **2012**, *14*, 8626-8632.
591   5.   Kołodziejczak-Radzimska, A.; Jesionowski, T. Zinc oxide—from synthesis to application: a review.
592   *Materials* **2014**, *7*, 2833–2881.
593   6.   Zhang, Y.; Ram, M. K.; Stefanakos, E. K.; Goswami, D. Y. Synthesis, characterization, and applications of
594   ZnO nanowires. *J. Nanomater.* **2012**, *2012*, 1–22.
595   7.   Naveed Ul Haq, A.; Nadhman, A.; Ullah, I.; Mustafa, G.; Yasinzai, M.; Khan, I. Synthesis Approaches of
596   Zinc Oxide Nanoparticles: The Dilemma of Ecotoxicity. *J. Nanomater.* 2017, 2017, 1–14.
597   8.   Cargnello, M.; Gordon, T. R.; Murray, C. B. Solution-phase synthesis of titanium dioxide nanoparticles and
598   nanocrystals. *Chem. Rev.* **2014**, *114*, 9319–9345.
599   9.   Znaidi, L. Sol–gel-deposited ZnO thin films: a review. *Mater. Sci. Eng. B* **2010**, *174*, 18–30.
600   10. Sepulveda-Guzman, S.; Reeja-Jayan, B.; de la Rosa, E.; Torres-Castro, A.; Gonzalez-Gonzalez, V.;
601   Jose-Yacaman, M. Synthesis of assembled ZnO structures by precipitation method in aqueous media.
602   *Mater. Chem. Phys.* **2009**, *115*, 172–178.
603   11. Oliveira, A. P. A.; Hochepied, J.-F.; Grillon, F.; Berger, M.-H. Controlled precipitation of zinc oxide
604   particles at room temperature. *Chem. Mater.* **2003**, *15*, 3202–3207.
605   12. Xi, Y.; Song, J.; Xu, S.; Yang, R.; Gao, Z.; Hu, C.; Wang, Z. L. Growth of ZnO nanotube arrays and nanotube
606   based piezoelectric nanogenerators. *J. Mater. Chem.* 2009, 19, 9260–9264.
607   13. Mulvihill, M. J.; Ling, X. Y.; Henzie, J.; Yang, P. Anisotropic etching of silver nanoparticles for plasmonic
608   structures capable of single-particle SERS. *J. Am. Chem. Soc.* **2010**, *132*, 268–274.
609   14. Li, F.; Ding, Y.; Gao, P.; Xin, X.; Wang, Z. L. Single-crystal hexagonal disks and rings of ZnO:
610   low-temperature, large-scale synthesis and growth mechanism. *Angew. Chem. Int. Ed.* **2004**, *43*, 5238–5242.
611   15. Tian, Z. R.; Voigt, J. A.; Liu, J.; Mckenzie, B.; Mcdermott, M. J.; Rodriguez, M. A.; Konishi, H.; Xu, H.
612   Complex and oriented ZnO nanostructures. *Nat. Mater.* **2003**, *2*, 821–826.
613   16. Mujtaba, J.; Sun, H.; Fang, F.; Ahmad, M.; Zhu, J. Fine control over the morphology and photocatalytic
614   activity of 3D ZnO hierarchical nanostructures: capping vs. etching. *RSC Adv.* **2015**, *5*, 56232–56238.
615   17. Malik, M. A.; Wani, M. Y.; Hashim, M. A. Microemulsion method: A novel route to synthesize organic and
616   inorganic nanomaterials. *Arabian J. Chem.* **2012**, *5*, 397–417.
617   18. Lin, J.-C.; Lee, C.-P.; Ho, K.-C. Zinc oxide synthesis via a microemulsion technique: morphology control
618   with application to dye-sensitized solar cells. *J. Mater. Chem.* **2012**, *22*, 1270–1273.
619   19. Demazeau, G. Solvothermal reactions: an original route for the synthesis of novel materials. *J. Mater. Sci.*
620   **2008**, *43*, 2104–2114.
621   20. Demazeau, G. Solvothermal processes: definition, key factors governing the involved chemical reactions
622   and new trends. *Zeitschrift für Naturforschung B* **2014**, *65*, 999–1006.
623   21. Feng, S.; Xu, R. New materials in hydrothermal synthesis. *Acc. Chem. Res.* **2001**, *34*, 239–247.
624   22. Shi, W.; Song, S.; Zhang, H. Hydrothermal synthetic strategies of inorganic semiconducting
625   nanostructures. *Chem. Soc. Rev.* **2013**, *42*, 5714–5743.
626   23. Hayashi, H.; Hakuta, Y. Hydrothermal synthesis of metal oxide nanoparticles in supercritical water.
627   *Materials* **2010**, *3*, 3794–3817.
628   24. Yang, H.; Song, Y.; Li, L.; Ma, J.; Chen, D.; Mai, S.; Zhao, H. Large-scale growth of highly oriented ZnO
629   nanorod arrays in the Zn-NH$_3$·H$_2$O hydrothermal system. *Cryst. Growth Des.* **2008**, *8*, 1039–1043.
630   25. Ko, S. H.; Lee, D.; Kang, H. W.; Nam, K. H.; Yeo, J. Y.; Hong, S. J.; Grigoropoulos, C. P.; Sung, H. J.
631   Nanoforest of hydrothermally grown hierarchical ZnO nanowires for a high efficiency dye-sensitized
632   solar cell. *Nano Lett.* **2011**, *11*, 666–671.
633   26. Joo, J.; Chow, B. Y.; Prakash, M.; Boyden, E. S.; Jacobson, J. M. Face-selective electrostatic control of
634   hydrothermal zinc oxide nanowire synthesis. *Nat. Mater.* **2011**, *10*, 596–601.
635   27. Zhao, X.; Lou, F.; Li, M.; Lou, X.; Li, Z.; Zhou, J. Sol–gel-based hydrothermal method for the synthesis of
636   3D flower-like ZnO microstructures composed of nanosheets for photocatalytic applications. *Ceram. Int.*
637   **2014**, *40*, 5507–5514.

638 28. Khan, M. F.; Ansari, A. H.; Hameedullah, M.; Ahmad, E.; Husain, F. M.; Zia, Q.; Baig, U.; Zaheer, M. R.;
639   Alam, M. M.; Khan, A. M.; AlOthman, Z. A.; Ahmad, I.; Ashraf, G. M.; Aliev, G. Sol-gel synthesis of
640   thorn-like ZnO nanoparticles endorsing mechanical stirring effect and their antimicrobial activities:
641   Potential role as nano-antibiotics. *Sci. Rep.* **2016**, 6, 27689/1-12.

642 29. Tseng, Y.-K.; Chuang, M.-H.; Chen, Y.-C.; Wu, C.-H. Synthesis of 1D, 2D, and 3D ZnO polycrystalline
643   nanostructures using the sol-gel method. *J. Nanotech.* **2012**, *2012*, 1–8.

644 30. Skompska, M.; Zarębska, K. Electrodeposition of ZnO nanorod arrays on transparent conducting
645   substrates–a review. *Electrochim. Acta* **2014**, *127*, 467–488.

646 31. Kumar, M.; Sasikumar, C. Electrodeposition of nanostructured ZnO thin film: a review. *Am. J. Mater. Sci.*
647   *Eng.* **2014**, *2*, 18–23.

648 32. Switzer, J. A.; Hodes, G. Electrodeposition and chemical bath deposition of functional nanomaterials. *MRS*
649   *Bulletin* **2010**, *35*, 743–750.

650 33. Bhattacharya, R. Chemical bath deposition, electrodeposition, and electroless deposition of
651   semiconductors, superconductors, and oxide materials. *In Solution Processing of Inorganic Materials*; Mitzi,
652   D. B., Ed.; John Wiley & Sons, Inc., **2008**; 199–237.

653 34. Choi, K.-S.; Jang, H. S.; McShane, C. M.; Read, C. G.; Seabold, J. A. Electrochemical synthesis of inorganic
654   polycrystalline electrodes with controlled architectures. *MRS Bulletin* **2010**, *35*, 753–760.

655 35. Lincot, D. Solution growth of functional zinc oxide films and nanostructures. *MRS Bulletin* **2010**, *35*,
656   778–789.

657 36. Illy, B. N.; Cruickshank, A. C.; Schumann, S.; Da Campo, R.; Jones, T. S.; Heutz, S.; McLachlan, M. A.;
658   McComb, D. W.; Riley, D. J.; Ryan, M. P. Electrodeposition of ZnO layers for photovoltaic applications:
659   controlling film thickness and orientation. *J. Mater. Chem.* **2011**, *21*, 12949-12957.

660 37. Oekermann, T.; Yoshida, T.; Schlettwein, D.; Sugiura, T.; Minoura, H. Photoelectrochemical properties of
661   ZnO/tetrasulfophthalocyanine hybrid thin films prepared by electrochemical self-assembly. *Phys. Chem.*
662   *Chem. Phys.* **2001**, *3*, 3387–3392.

663 38. Shi, Z.; Walker, A. V. Chemical Bath Deposition of ZnO on Functionalized self-assembled monolayers:
664   selective deposition and control of deposit morphology. *Langmuir* **2015**, *31*, 1421–1428.

665 39. Hodes, G. Semiconductor and ceramic nanoparticle films deposited by chemical bath deposition. *Phys.*
666   *Chem. Chem. Phys.* **2007**, *9*, 2181-2196.

667 40. She, G.-W.; Zhang, X.-H.; Shi, W.-S.; Fan, X.; Chang, J. C.; Lee, C.-S.; Lee, S.-T.; Liu, C.-H. Controlled
668   synthesis of oriented single-crystal ZnO nanotube arrays on transparent conductive substrates. *Appl. Phys.*
669   *Lett.* 2008, *92*, 053111/1-3.

670 41. Xu, L.; Liao, Q.; Zhang, J.; Ai, X.; Xu, D. Single-crystalline ZnO nanotube arrays on conductive glass
671   substrates by selective disolution of electrodeposited ZnO nanorods. *J. Phys. Chem. C* **2007**, *111*, 4549–4552.

672 42. Hu, L.; Hu, Z.; Liu, C.; Yu, Z.; Cao, X.; Han, Y.; Jiao, S. Electrochemical assembly of ZnO architectures via
673   deformation and coalescence of soft colloidal templates in reverse microemulsion. *RSC Adv.* **2014**, *4*,
674   24103–24109.

675 43. Zhai B.; Huang Y.-M. A review on recent progress in ZnO based photocatalysts. *Optoelectronic Mater.* **2016**,
676   1, 22-36.

677 44. Xia, Y.; Wang, J.; Chen, R.; Zhou, D.; Xiang, L. A review on the fabrication of hierarchical ZnO
678   nanostructures for photocatalysis application. *Crystals* **2016**, *6*, 148/1-19.

679 45. Hezam, A.; Namratha, K.; Drmosh, Q. A.; Chandrashekar, B. N.; Sadasivuni, K. K.; Yamani, Z. H.; Cheng,
680   C.; Byrappa, K. Heterogeneous growth mechanism of ZnO nanostructures and the effects of their
681   morphology on optical and photocatalytic properties. *CrystEngComm* **2017**, *19*, 3299–3312.

682 46. Xiaoliang, W.; Shihua, D.; Yong, P.; Qin, X.; Yun, L. Study of the photocatalytic activity of Na and
683   Al-doped ZnO Ppowders. *Ferroelectrics* **2013**, *455*, 90–96.

684 47. Kurbanov, S.; Yang, W. C.; Kang, T. W. Kelvin probe force microscopy of defects in ZnO nanocrystals
685   associated with emission at 3.31 eV. *Appl. Phys. Express* **2011**, *4*, 021101/1-3.

686 48. Mohd, A. M. A.; Julkapli, N. M.; Abd, H. S. B. Review on ZnO hybrid photocatalyst: impact on
687   photocatalytic activities of water pollutant degradation. *Rev. Inorg. Chem.* **2016**, *36*, 77–104.

688 49. Kumar, S. G.; Rao, K. S. R. K. Zinc oxide based photocatalysis: tailoring surface-bulk structure and related
689   interfacial charge carrier dynamics for better environmental applications. *RSC Adv.* **2015**, 5, 3306–3351.

690   50. Ahmad, M.; Yingying, S.; Nisar, A.; Sun, H.; Shen, W.; Wei, M.; Zhu, J. Synthesis of hierarchical flower-like
691   ZnO nanostructures and their functionalization by Au nanoparticles for improved photocatalytic and high
692   performance Li-ion battery anodes. *J. Mater. Chem.* **2011**, *21*, 7723-7729.
693   51. Sui, M.; Gong, P.; Gu, X. Review on one-dimensional ZnO nanostructures for electron field emitters. *Front.*
694   *Optoelectron.* **2013**, *6*, 386–412.
695   52. Semet, V.; Adessi, C.; Capron, T.; Thien Binh, V. Electron emission from low surface barrier cathodes. *J. Vac.*
696   *Sci. Technol. B* **2007**, *25*, 513-516.
697   53. Xu, N. S.; Huq, S. E. Novel cold cathode materials and applications. *Mater. Sci. Eng. R* **2005**, *48*, 47–189.
698   54. Cui, J. B.; Daghlian, C. P.; Gibson, U. J.; Püsche, R.; Geithner, P.; Ley, L. Low-temperature growth and field
699   emission of ZnO nanowire arrays. *J. Appl. Phys.* **2005**, *97*, 044315/1-7.
700   55. Liu, J.; Huang, X.; Li, Y.; Ji, X.; Li, Z.; He, X.; Sun, F. Vertically aligned 1D ZnO nanostructures on bulk alloy
701   substrates: direct solution synthesis, photoluminescence, and field emission. *J. Phys. Chem. C* **2007**, *111*,
702   4990–4997.
703   56. Dev, A.; Kar, S.; Chakrabarti, S.; Chaudhuri, S. Optical and field emission properties of ZnO nanorod
704   arrays synthesized on zinc foils by the solvothermal route. *Nanotechnology* **2006**, *17*, 1533-1540.
705   57. Wei, A.; Sun, X. W.; Xu, C. X.; Dong, Z. L.; Yu, M. B.; Huang, W. Stable field emission from hydrothermally
706   grown ZnO nanotubes. *Appl. Phys. Lett.* **2006**, *88*, 213102/1-3.
707   58. Cao, B.; Cai, W.; Duan, G.; Li, Y.; Zhao, Q.; Yu, D. A template-free electrochemical deposition route to ZnO
708   nanoneedle arrays and their optical and field emission properties. *Nanotechnology* **2005**, *16*, 2567-2574.
709   59. Ma, H.; Qin, Z.; Wang, Z.; Ahmad, M.; Sun, H. Enhanced field emission of ZnO nanoneedle arrays via
710   solution etching at room temperature. *Mater. Lett.* **2017**, *206*, 162–165.
711   60. Su, X.-F.; Chen, J.-B.; He, R.-M.; Li, Y.; Wang, J.; Wang, C.-W. The preparation of oxygen-deficient ZnO
712   nanorod arrays and their enhanced field emission. *Mater. Sci. Semicon. Proc.* **2017**, *67*, 55–61.
713   61. Mahmood, K.; Park, S. B.; Sung, H. J. Retracted Article: Enhanced photoluminescence, Raman spectra and
714   field-emission behavior of indium-doped ZnO nanostructures. *J. Mater. Chem. C* **2013**, *1*, 3138–3149.
715   62. Shao, D.; Gao, J.; Xin, G.; Wang, Y.; Li, L.; Shi, J.; Lian, J.; Koratkar, N.; Sawyer, S. Cl-doped ZnO nanowire
716   arrays on 3D graphene foam with highly efficient field emission and photocatalytic properties. *Small* **2015**,
717   *11*, 4785–4792.
718   63. Yang, K.; She, G.-W.; Wang, H.; Ou, X.-M.; Zhang, X.-H.; Lee, C.-S.; Lee, S.-T. ZnO nanotube arrays as
719   biosensors for glucose. *J. Phys. Chem. C* **2009**, *113*, 20169–20172.
720   64. Cosentino, S.; Fiaschi, G.; Strano, V.; Hu, K.; Liao, T.-W.; Hemed, N. M.; Yadav, A.; Mirabella, S.;
721   Grandjean, D.; Lievens, P.; Shacham-Diamand, Y. Role of Au_xPt_{1-x} clusters in the enhancement of the
722   electrochemical activity of ZnO nanorod electrodes. *J. Phys. Chem. C* **2017**, *121*, 15644–15652.
723   65. Meng, S.; Hong, Y.; Dai, Z.; Huang, W.; Dong, X. Simultaneous detection of dihydroxybenzene isomers
724   with ZnO nanorod/carbon cloth electrodes. *ACS Appl. Mater. Interfaces* **2017**, *9*, 12453–12460.
725   66. Hussain, M.; Sun, H.; Karim, S.; Nisar, A.; Khan, M.; ul Haq, A.; Iqbal, M.; Ahmad, M. Noble metal
726   nanoparticle-functionalized ZnO nanoflowers for photocatalytic degradation of RhB dye and
727   electrochemical sensing of hydrogen peroxide. *J. Nanopart. Res.* **2016**, 18, 95/1-14.
728   67. Wang, H.; Pan, Q.; Cheng, Y.; Zhao, J.; Yin, G. Evaluation of ZnO nanorod arrays with dandelion-like
729   morphology as negative electrodes for lithium-ion batteries. *Electrochim. Acta* **2009**, *54*, 2851–2855.
730   68. Xiao, C.; Zhang, S.; Wang, S.; Xing, Y.; Lin, R.; Wei, X.; Wang, W. ZnO nanoparticles encapsulated in a 3D
731   hierarchical carbon framework as anode for lithium ion battery. *Electrochim. Acta* 2016, 189, 245–251.
732   69. Zhang, J.; Gu, P.; Xu, J.; Xue, H.; Pang, H. High performance of electrochemical lithium storage batteries:
733   ZnO-based nanomaterials for lithium-ion and lithium–sulfur batteries. *Nanoscale* **2016**, *8*, 18578–18595.
734   70. Sun, Y.; Liu, N.; Cui, Y. Promises and challenges of nanomaterials for lithium-based rechargeable batteries.
735   *Nat. Energy* **2016**, *1*, 16071/1-12.
736   71. Yu, S.-H.; Lee, S. H.; Lee, D. J.; Sung, Y.-E.; Hyeon, T. Conversion reaction-based oxide nanomaterials for
737   lithium ion battery anodes. *Small* **2016**, *12*, 2146–2172.
738   72. Xu, X.; Cao, K.; Wang, Y.; Jiao, L. 3D hierarchical porous $ZnO/ZnCo_2O_4$ nanosheets as high-rate anode
739   material for lithium-ion batteries. *J. Mater. Chem. A* **2016**, *4*, 6042–6047.
740   73. Chen, H.; Ding, L.-X.; Xiao, K.; Dai, S.; Wang, S.; Wang, H. Highly ordered $ZnMnO_3$ nanotube arrays from
741   a "self-sacrificial" ZnO template as high-performance electrodes for lithium ion batteries. *J. Mater. Chem. A*
742   **2016**, *4*, 16318–16323.

743   74.   Kim, J.; Hong, S.-A.; Yoo, J. Continuous synthesis of hierarchical porous ZnO microspheres in supercritical
744   methanol and their enhanced electrochemical performance in lithium ion batteries. *Chem. Eng. J.* **2015**, *266*,
745   179–188.
746   75.   Chen, Y.; Du, N.; Zhang, H.; Yang, D. Porous Si@C coaxial nanotubes: layer-by-layer assembly on ZnO
747   nanorod templates and application to lithium-ion batteries. *CrystEngComm* **2017**, *19*, 1220–1229.
748   76.   Yuan, C.; Cao, H.; Zhu, S.; Hua, H.; Hou, L. Core–shell $ZnO/ZnFe_2O_4@C$ mesoporous nanospheres with
749   enhanced lithium storage properties towards high-performance Li-ion batteries. *J. Mater. Chem. A* **2015**, *3*,
750   20389–20398.
751   77.   Zhang, L.; He, W.; Liu, Y.; Zheng, P.; Yuan, X.; Guo, S. Temperature effect on morphology and
752   electrochemical properties of nanostructured ZnO as anode for lithium ion batteries. *IET Micro Nano*
753   *Letters* **2016**, *11*, 535–538.
754   78.   Lu, S.; Wang, H.; Zhou, J.; Wu, X.; Qin, W. Atomic layer deposition of ZnO on carbon black as
755   nanostructured anode materials for high-performance lithium-ion batteries. *Nanoscale* **2017**, *9*, 1184–1192.
756   79.   Gao, S.; Fan, R.; Li, B.; Qiang, L.; Yang, Y. Porous carbon-coated ZnO nanoparticles derived from low
757   carbon content formic acid-based Zn(II) metal-organic frameworks towards long cycle lithium-ion anode
758   material. *Electrochim. Acta* **2016**, *215*, 171–178.
759   80.   Xie, Q.; Lin, L.; Ma, Y.; Zeng, D.; Yang, J.; Huang, J.; Wang, L.; Peng, D.-L. Synthesis of ZnO-Cu-C
760   yolk-shell hybrid microspheres with enhanced electrochemical properties for lithium ion battery anodes.
761   *Electrochim. Acta* **2017**, *226*, 79–88.
762   81.   Yang, X.; Xue, H.; Yang, Q.; Yuan, R.; Kang, W.; Lee, C.-S. Preparation of porous $ZnO/ZnFe_2O_4$ composite
763   from metal organic frameworks and its applications for lithium ion batteries. *Chem. Eng. J.* **2017**, *308*,
764   340–346.
765   82.   Quartarone, E.; Dall'Asta, V.; Resmini, A.; Tealdi, C.; Tredici, I. G.; Tamburini, U. A.; Mustarelli, P.
766   Graphite-coated ZnO nanosheets as high-capacity, highly stable, and binder-free anodes for lithium-ion
767   batteries. *J. Power Sources* **2016**, *320*, 314–321.
768   83.   Ge, X.; Li, Z.; Wang, C.; Yin, L. Metal–organic frameworks derived porous core/shell structured
769            $ZnO/ZnCo_2O_4/C$ hybrids as anodes for high-performance lithium-ion battery. *ACS Appl. Mater. Inter.* **2015**,
770   *7*, 26633–26642.
771   84.   Zhang, G.; Hou, S.; Zhang, H.; Zeng, W.; Yan, F.; Li, C. C.; Duan, H. High-performance and ultra-stable
772   lithium-ion batteries based on MOF-derived ZnO@ZnO quantum dots/C core-shell nanorod arrays on a
773   carbon cloth anode. *Adv. Mater.* **2015**, *27*, 2400–2405.
774   85.   Xu, F.; Li, Z.; Wu, L.; Meng, Q.; Xin, H. L.; Sun, J.; Ge, B.; Sun, L.; Zhu, Y. In situ TEM probing of
775   crystallization form-dependent sodiation behavior in ZnO nanowires for sodium-ion batteries. *Nano*
776   *Energy* 2016, 30, 771–779.
777   86.   Asayesh-Ardakani, H.; Yao, W.; Yuan, Y.; Nie, A.; Amine, K.; Lu, J.; Shahbazian-Yassar, R. In Situ TEM
778   Investigation of ZnO Nanowires during Sodiation and Lithiation Cycling. *Small Methods* 2017, 1, 1700202.